JES Focus Issue of Selected Papers from IMLB 2018

Mesopore Channel Length Control in Ordered Mesoporous Carbon Hosts for High Performance Lithium-Sulfur Batteries

Byong-June Lee,[1,=] Hyean-Yeol Park,[1,2,=] Dae-Soo Yang,[1] Tong-Hyun Kang,[1] Seongpil Hwang,[2,z] and Jong-Sung Yu[1,z]

[1]*Department of Energy Science and Engineering, Daegu Gyeongbuk Institute of Science and Technology (DGIST), Daegu 42988, Korea*
[2]*Department of Advanced Materials Chemistry, Korea University, Sejong 30019, Korea*

Ordered mesoporous carbons (OMCs) with different mesopore channel length, prepared by using corresponding size-tuned ordered mesoporous silicas as templates, are explored as hosts for sulfur (S) in cathode to investigate the effect of the mesopore length on Li-S battery (LSB) performance. The well-developed mesopores in the OMCs provide an excellent ion transport path, enhancing mass transport capability and thus demonstrating better cycling performance and rate capability. Particularly, platelet OMC (pOMC) with thin hexagonal prism shape and short mesopore length demonstrates the high reversible discharge capacity of 1419 mAh g^{-1} at a current density of 168 mA g^{-1} and excellent cyclability. Based on the specific capacity, cycle efficiency, and rate capability, the pOMC-S outperforms considerably its mesoporous carbon peers, rod-like OMC-S (rOMC-S) and spherical OMC-S (sOMC-S) with longer mesopore length. This superb behavior is attributed to better and more utilization of short mesopore channels for active sulfur species, which induce higher sulfur utilization, and are also supported by low electrochemical resistances in electrochemical impedance spectroscopy. The improved cell performance can be understood in terms of utilization efficiency of the mesopore channels for sulfur loading and polysulfide dissolution, which improves with decreasing channel length.
 [DOI: 10.1149/2.0391903jes]

Manuscript submitted October 9, 2018; revised manuscript received December 10, 2018. Published December 28, 2018. *This paper is part of the JES Focus Issue of Selected Papers from IMLB 2018.*

The increasing demand for high energy density devices has prompted the intense efforts toward development of new electrode materials with high energy capacity for rechargeable lithium ion batteries (LIBs).[1,2] In particular, lithium-sulfur battery (LSB) has been considered as a new generation battery with high energy density because sulfur cathode has a high theoretical capacity of 1675 mAh g^{-1} and a high theoretical energy density of 2600 Wh kg^{-1}, which is about 3–5 times higher than those of commercial cathode materials in current state-of-the-art LIB.[3,4] Moreover, the abundance of sulfur in nature offers other advantages such as low cost, low equivalent weight, and environmental friendliness, which cannot only make it a prospective choice for wide applications but also reduce the cost of Li batteries.[5,6] The electrochemical reaction in LSBs occurs between metallic Li in anode and sulfur in cathode. In discharge process, metallic lithium is oxidized to generate electron and Li^+ at anode, while at cathode, solid-phase sulfur reacts with the electron and Li^+ to form highly soluble lithium polysulfides (Li_2S_n, $4 \leq n \leq 8$). In subsequent process, the soluble lithium polysulfides are further reduced to solid-phase Li_2S and Li_2S. In charge process, reverse reaction converts the Li_2S back to lithium polysulfides (Li_2S_n, $4 \leq n \leq 8$) and further to S_8.

However, despite many attractive properties, LSBs suffer from several issues. One issue is related to the soluble lithium polysulfide intermediates generated during electrochemical reaction, which can lead to low sulfur utilization and poor cyclability of the active material in the electrodes. The lithium polysulfides (Li_2S_n, $4 \leq n \leq 8$) formed during cycles are dissolved in electrolyte solution, and their diffusion and shuttle phenomenon result in poor cyclability, severe lithium anode corrosion, and low Coulombic efficiency.[7,8] Another issue is the low conductivity of sulfur (5×10^{-30} S cm^{-1} at 25°C) and its reduced polysulfides, which need conductive medium around them for electrochemical reactions. The volumetric expansion of polysulfide intermediates (~80% increase from S to Li_2S) during cycles may also cause the instability of cathode structure.[9–11]

To overcome the above challenges, considerable attempts have been made to encapsulate S into various carbonaceous host materials, which cannot only improve the electrical conductivity but also suppress the dissolution/diffusion issues of polysulfide intermediates during cycles. Many types of carbon host materials such as carbon nanofibers,[12,13] carbon nanotubes,[14–16] carbon spheres,[17,18] porous carbon,[10,19] and graphene sheets[20–23] have been reported as conductive pathways for S, and greatly improved cyclability and rate capability in comparison with pristine S. Their high specific surface areas, high pore volumes and good adsorption ability contribute to the decrease of the diffusion into electrolyte and the shuttle of polysulfides.[7]

Based on various literature reports in the past several years, an ideal S host materials should satisfy the several characteristics,[24] such as sufficient space to accommodate S volumetric expansion, short transport pathways for both lithium ions and electrons to improve the capacity and power capability, and a high surface area for effective encapsulation of S and intermediate polysulfides in order to preserve the morphology of the electrode.[25] Moreovere, the pore structure and size of porous carbon as a sulfur host are also important factors that determine the electrochemical activity and cycling stability of the carbon-sulfur composite cathode.[4,26]

Ordered mesoporous carbon (OMC) is usually synthesized by nanocasting method that employs corresponding ordered mesoporous silica (OMS) as a hard template, and possesses several advantageous properties such as a large surface area and pore volume, tunable pore size and uniform structure.[27–29] Thus, the OMC has been widely used for many applications in electrocatalysis, LIB and supercapacitor electrodes. Nazar et al. reported that a sulfur-carbon composite including CMK-3, one of OMC materials as a host, could achieve a great improvement in the electrochemical utilization and cyclability of sulfur.[10] The morphology of OMC can be tailored by regulating the size and shape of parent OMS, which can be controlled from rod-like morphology to sherical and prism-like morphologies and to other shapes through changing chemical synthesis conditions.[30] In particular, a thin plate- or disk-like OMC (pOMC) is a new development with short mesopore channel length among various types of OMC materials.[31,32] Interestingly, this shape and size tuning changes

[=]These authors contributed equally to this work.
[z]E-mail: jsyu@dgist.ac.kr; sphwang@korea.ac.kr

the specific surface area and mesopore volume of OMCs. With the shorter channel length of OMCs, generally the higher surface area and pore volume are obtained.[33] In this work, we have designed the OMCs with various sizes and morphologies through nanocasting method of the corresponding OMS structures and explored them as host materials for sulfur in LSB. Interestingly, the capacity, cycle efficiency, and rate capability are found to be related to the mesopore channel length of the OMCs. The pOMC material possesses excellent surface properties like shorter mesopore channels and higher surface area compared to conventional rod-like OMC, which can greatly facilitate Li ion diffusion and electrolyte transport and correspondingly induce better sulfur utilization to enhance Li storage capacity, cycle efficiency, and rate capability.

Experimental

Synthesis of OMC materals.—The ordered mesoporous carbon (OMC) was synthesized by a nanocasting method using corresponging ordered mesoporous silica (OMS) as a hard template and phenol/paraformaldehyde resin as carbon precursor. The OMS samples can be produced with rod-like shape, and the length can be controled through regulation of HCl concentration under hydrothermal reaction conditions according to the reported procedures.[30,34] On the other hand, platelet-like mesoporous silica (pOMS) with very short mesopore length was synthesized through modification of a previously reported procedure.[31,32] In a typical process of OMS, 1.0 g of Pluronic P123 surfactant (Aldrich, Mn = 5800) was dissolved in 40 g of 2.0 M HCl aqueous solution and allowed to stir for 3 h at 35°C. Once the solution became clear, 2.25 mL of tetraethyl orthosilicate (TEOS, Aldrich, 98%) was added, and so-formed colloidal suspension was kept being stirred at the same temperature for 24 h. After that, the reaction mixture was transferred to a polytetrafluoroethylene (PTFE) vessel, which was then sealed and heated at 90°C for 24 h in an oven without any stirring. For a platelet OMS, 0.161 g of $ZrOCl_2 \bullet 8H_2O$ (Sigma-Aldrich, 99.5%) along with 2.25 mL of tetraethyl orthosilicate (TEOS, Aldrich, 98%) is added to the above-mentioned Pluronic P123 surfactant solution. The remaining process was preformed through the identical syntheis procedure. The resulting product was retrieved by fltration, followed by washing with deionized water and drying in an oven at 80°C. The as-synthesized platelet-like and rod-like OMS samples with different mesopore length were then calcined in air at 550°C for 12 h in order to remove the remaining surfactant in the main channels.

A typical synthesis route for OMCs is as follows. 0.374 g of phenol was introduced into 1.0 g of OMS template by heating at 100°C for 12 h under vacuum. The resulting phenol-incorporated OMS template was then reacted with paraformaldehyde (0.238 g) under vacuum at 130°C for 24 h to produce a composite of phenol-paraformaldehyde resin/OMS. The resultant resin/OMS composite was heated under N_2 gas flow to 900°C at a ramping rate of 5°C min^{-1}, and then heated at 900°C for 5h in order to induce carbonization of the cross-linked phenol resin inside the mesopores of the OMS structure in N_2 flow. After carbonization and natural cooling to ambient temperature, silica template was removed by dissolving in 3.0 M NaOH in an oven at 80°C overnight to get silica-free OMC. The samples thus-obtained were filtered, washed with ethanol and dried at 80°C. Different types of silica-free OMCs with different mesopore length were termed rod-type OMC (rOMC), spherical-type OMC (sOMC), and platelet-type OMC (pOMC) based on their shape as illustrated in Figure S1.

Synthesis of OMC-S composite.—The OMC-S composite was prepared by following a conventional melting-diffusion strategy. The as-prepared OMC-sulfur composite with 4:6 weight ratios (OMC:S = 4:6) was grinded together, transferred to a Teflon pot, and heated at 155°C for 12 h. Most of the S was infiltrated into the pores of OMC, but some amount of S might adhere to the surface of OMC. Each of the OMC-S composites was further heated at 250°C for 3 h under a N_2 atmosphere in a closed vial to ensure homogeneous distribution of S inside the mesopores, and then, a final OMC-S composite was attained after cooling down.

Materials characterization.—The morphologies and structures of as-prepared OMC materials and OMC-sulfur composites with different molphology were further characterized using using high resolution scanning electron microscopy (HR-SEM) and high resolution transmission electron microscopy (HR-TEM). HR-SEM analysis was carried out using a Hitachi S-5500 microscope operated at 30 kV. HR-TEM images were obtained using a JEOL FE-2010 microscope operated at 200 kV. The phase analyses of OMC materials and OMC-S composite were confirmed by wide angle X-ray diffraction (XRD) and small angle X-ray scattering (SAXS) measurements using Rigaku 1200 with Cu-Kα radiation and a Ni β-filter operating at 40 kV and 20 mA. The amount of sulfur loading in OMC-S composite sample was measured by thermogravimatric analysis (TGA) using Bruker TG-DTA2000SA analyzer. N2 adsorption-desorption isotherms were measured at −196°C on micromeritics ASAP 2020 surface area and porosity analyzer after the sample was degassed at 60°C to 20 mTorr for 1 h. The specific surface area was determined from nitrogen adsorption using Brunauer-Emmett-Teller (BET) equation along with pore size distribution (PSD) from Barrett-Joyner-Halenda (BJH) and cumulative pore volume from density functional theory (DFT) method.

Electrochemical performance measurement.—The electrochemical measurements were carried out with 2025 coin cells assembled in an argon-filled glove box with OMC-S composite as a cathode electrode and lithium metal as reference and counter electrode. The electrodes in a cell were separated by a Celgard 2400 separator. Electrolyte used in the cell was prepared by adding 1.0 M lithium bistrifluoromethanesulfonylimide in a mixture of 1,3-dioxolane (DOL) and dimethoxyethane (DME) (1:1 by volume) with 0.2 M $LiNO_3$ additive.[35] The rate set for cell test was referenced to the mass of sulfur active material in the cathode, and 1 C equaled to 1675 mA g^{-1}. The charge–discharge behavior of the coin cell was characterized in a BaSyTec multichannel battery test system at a constant room temperature. The instrument was programmed to read in each 10 s step. The cell was cycled in the voltage range of 1.8–2.8 V at a rate of 100 mA g^{-1} during an initial process and at different rates in the following cycles. Cyclic voltamogram (CV) measurement was conducted with a scan rate of 0.1 mV s^{-1}, and electrochemical impedence spectroscopy (EIS) measurement was carried out in the frequency range of 100 mHz to 10 kHz with a zero-bias potential and 10 mV of amplitude. Impedance spectrum was analyzed by fitting the spectra to the proposed equivalent circuit using Zview software.

Results and Discussion

Structural analysis of OMC-S composites.—Figure 1a illustrates the formation procedure of pOMC-S composite and its electrochemical process. The mesopores of OMC are gradually filled with sulfur due to the lowest surface tension of sulfur at 155°C.[36] During discharge reaction, solid sulfur, S_8 in OMC is reduced by lithium, and the sulfur chain length is gradually shortened until the final discharge product Li_2S is formed. The overall redox couple of a lithium-sulfur cell is described by the reaction $S_8 + 16Li \leftrightarrow 8Li_2S$ and occurs at a potential of 2.15 V vs. Li/Li^+.

The structure and morphologies of the as-synthesized OMC materials were characterized by SEM and TEM measurements in Figure S2. TEM images of the OMCs show the formation of highly ordered uniform mesopores in the carbon framework. All the OMCs were prepared from the corresponding OMS templates with different morphologies and mesopore channel length. The definition of channel length and cross-sectional diameter used to describe the OMCs is illustrated in Figure S1. The rOMC illustrates a rod-like carbon structure with an average mesopore length of ca. 0.10 um and a cross-sectional diameter of ca. 0.4 um with an aspect ratio of ∼2.5. The mesopore channel length can be controlled in rod-like OMC, and as the mesopore length decreases, the cross-sectional diameter increases.

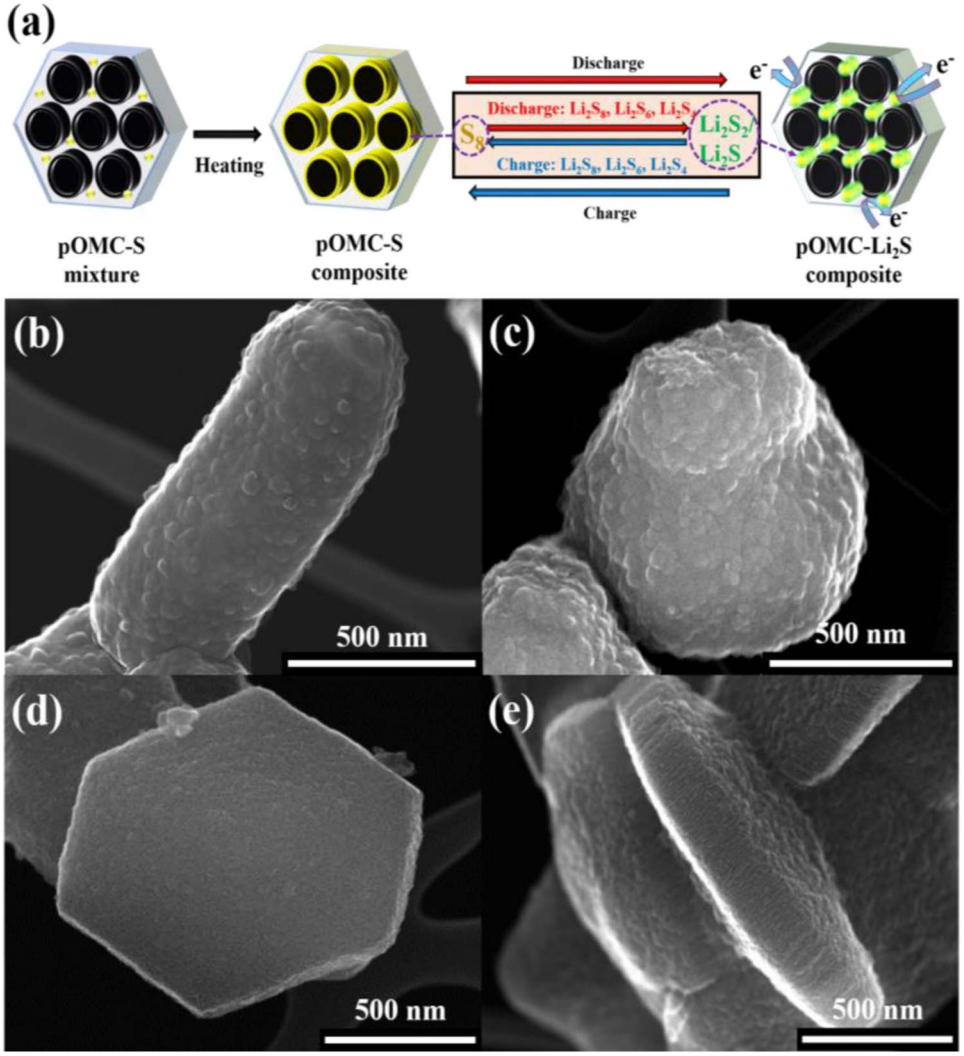

Figure 1. (a) Schematic illustration of the electrode structure and its electrochemical processes. SEM images of OMC-S composites with various morphology and channel length: (b) rOMC-S, (c) sOMC-S, (d) top and (e) lateral side view of pOMC-S.

Thus, sOMC, where the mesopore length becomes almost identical to cross-sectional diameter (0.6 nm), shows spherical shape with an aspect ratio of ∼1. The mesopore length can be shrunken furthermore, and then, thin hexagonal prism-like morphology with short mesopore channel length can be obtained in the case of pOMC with an average mesopore length of ca. 0.2 um and a cross-sectional diameter of ca. 1.2 um with an aspect ratio of ∼0.17. In particular, the uniform hexagonal platelet morphology represents near perfect crystal growth expected from crystal growth of hexagonal unit cell structure.

After sulfur is infiltrated into the OMCs, the SEM images of three differently sized OMC-S composites are shown in Figures 1b–1e. TEM images of the OMC-S composites show ordered mesopore arrays in Figure 2. All the OMC-S composites maintains the original shape and dimension, illustrating the robustness of the OCM hosts for sulfur loading. Interestingly, the inner parts of rOMC-S and sOMC-S composites have much lighter color compared to the outer parts on the surface as seen in TEM images of Figure 2. This may indicate that sulfur can more densely loaded only on the mesopore channel parts near on the surface since the OMCs have longer mesopore channels, which cannot be fully filled with sulfur. The sulfur densely loaded near on the surface may also black the way to inner part so that densely sulfur-loaded shell and empty or less-populated core zone may form as seen in rOMC-S and sOMC-S composites in Figures 2a and 2b. The rOMC-S composite with long mesopore channel length clearly

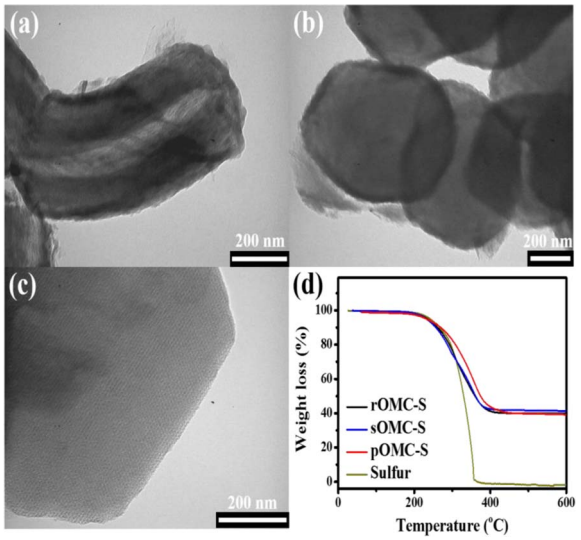

Figure 2. TEM images of as-prepared (a) rOMC-S, (b) sOMC-S, and (c) pOMC-S. (d) TGA curves of pure S, rOMC-S, sOMC-S, and pOMC-S composites under a N_2 atmosphere.

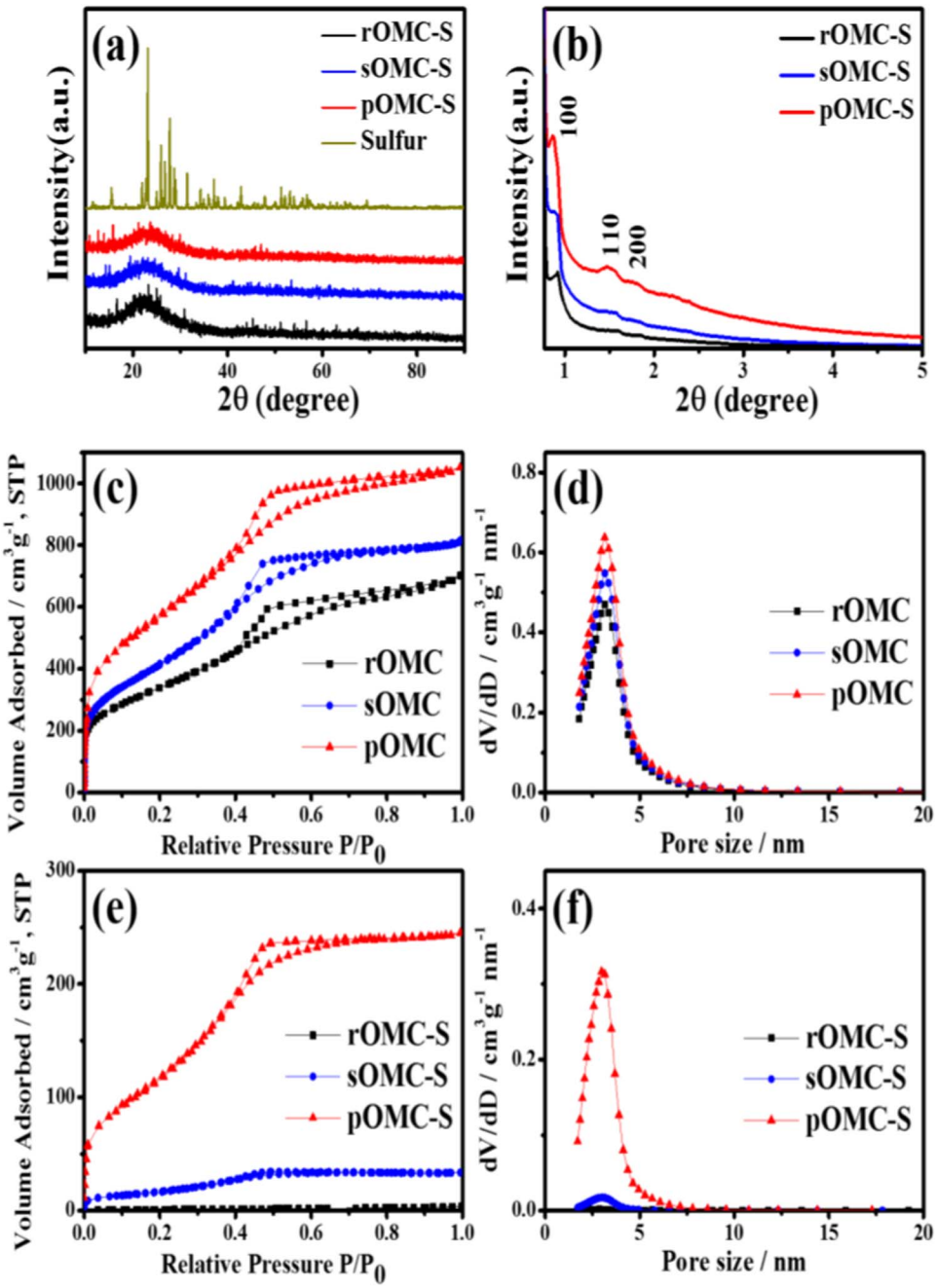

Figure 3. (a) Wide-angle and (b) small-angle XRD patterns of various OMC-S composites. (c) N_2 sorption isotherms and (d) pore size distribution of sulfur-free OMCs with different channel length. (e) N_2 sorption isotherms and (f) pore size distribution of the corresponding OMC-S composites.

reveals empty core zone not occupied by sulfur along with thicker shell with high sulfur loading. The shell thickness decreases with decreasing mesopore channel length since more sulfur can travel into the inner part with decreasing channel length as seen for rOMC-S and sOMC-S in Figures 2a and 2b. On the other hand, interestingly, such densely populated shell structure cannot be seen in the TEM image of pOMC composite probably due to easy filling of sulfur into short mesopore channels. (Figure 2c).

The thermogravimetric analysis (TGA) under N_2 atmosphere was measured to determine the S content in various OMC-S composites in Figure 2d. The TGA curves show one weight loss stage from around 200 to 400°C, indicating the evaporation of S from the respective OMC framework. Interestingly, the sulfur in pOMC-S illustrates a bit better stability, which indicates relatively better distribution of sulfur throughout the porous structure unlike high localized distribution near at the surface for rOMC-S and sOMC-S. For the three OMC-S composites, the S weight percentage ranges from 59 to 62%, i.e. about 60 wt% sulfur loading for all the OMC-S composites.

Figure 3a shows the wide-angle XRD patterns of S and various OMC-S composites. Bare sulfur illustrate typical sharp lines in the XRD measurement. All the OMC-S composites show a broad signal near at $2\Theta = 22$, which corresponds to amorphous carbon framework. Several short sharp lines, which may correspond to some sulfur species are still observed in all the OMC-S composites. The small-angle XRD patterns in Figure 3b indicate that all the OMC-S composites contain three diffraction peaks corresponding to the (100), (110), and (200) planes typical of 2D hexagonal *p6mm* pore structure. The low-angle (100) diffraction peaks at $2\Theta = 0.94$, 0.92, and 0.90 for rOMC-S,

Table I. Structural properties of various types of OMCs and OMC-S composites.

Sample	S_{BET} ($m^2\ g^{-1}$)	V_{total} ($cm^3\ g^{-1}$)	V_{micro} ($cm^3\ g^{-1}$)	V_{meso} ($cm^3\ g^{-1}$)	PSD (nm)
rOMC	1077	1.78	0.74	1.04	3.2
sOMC	1274	2.08	0.79	1.29	3.3
pOMC	1687	3.24	1.47	1.77	3.3
rOMC-S	5	0.0072	0.0007	0.0065	2.8
sOMC-S	78	0.07	0.01	0.06	2.9
pOMC-S	384	0.86	0.25	0.61	3.0

sOMC-S, and pOMC-S, respectively, confirm the ordered mesoporous structure of the as-synthesized OMCs. Interestingly, the (100) peak shift toward lower angle is related to the increase in mesopore size with decreasing mesopore channel length of the OMCs. The (100) peak intensity decreases more with increasing mesopore length probably due to thick heavily sulfur-loaded shell area as shown in Figure 2a.

N_2 adsorption-desorption isotherms were measured before and after S infiltration into mesoporous carbon as shown in Figures 3c and 3e to determine the surface properties of the OMCs. Although after sulfur loading, the isotherm intensity drastically deceases due to pore filling with sulfur, all the OMCs and OMC-S composites show similar isotherm profiles characteristic of type IV with H2-type hysteresis loop, suggesting uniform mesoporous structure for both OMC and corresponding OMC-S composite. As shown in Figure 3d, all three OMC materials reveal a similar pore size distribution with uniform mesopores averaged at 3.3 nm. Furthermore, BET surface areas were also determined along with pore size distribution (PSD) and cumulative pore volume. The detailed surface parameters for all the OMCs and the OMC-S composites are summarized in Table I. Interestingly, surface area and mesopore volume is found to increase with the decreasing mesopore channel length in OMC framework. The surface area and total pore volume were determined to be ca. 1687 $m^2\ g^{-1}$ and ca. 3.24 $cm^3\ g^{-1}$ for the pOMC, respectively, which were much higher than those observed for the rOMC (ca. 1077 $m^2\ g^{-1}$ and ca. 1.78 $cm^3\ g^{-1}$) and the sOMC (ca. 1274 $m^2\ g^{-1}$ and ca. 2.08 $cm^3\ g^{-1}$). Compared with bare OMCs, the OMC-S composites illustrates decreased N_2 adsorption volume as shown in Figure 3e, indicating decreased surface properties. As expected, the surface areas of corresponding OMC-S composites significantly decreased to nearly ~5 $m^2\ g^{-1}$ for rOMC-S and ca. 78 $m^2\ g^{-1}$ for sOMC-S for 60 wt% S loading, indicating that most of the pores are almost completely filled. The mesopores are also significantly diminished for rOMC-S and sOMC-S composites as indicated by mesopore peak internsity in Figure 3f, indicating faithful loading of sulfur into the mesopores of the OMCs. On the other hand, interestingly, the pOMC-S composite with identical 60 wt% S loading still holds some surface area and the pore volume of ca. 384 $m^2\ g^{-1}$ and ca. 0.86 $cm^3\ g^{-1}$, respectively. This indicates that the pOMC-S composite still maintains about 23% of the initial mespore surface area along with only slightly decreased PSD compared to the bare pOMC, suggesting that sulfur is not distributed homogeneously in the porous carbon framework. Some parts are fully filled, but other parts are only partially filled with sulfur. This may infer that about 77% of mesopores is almost completely filled with sulfur, while the remaining 23% is only partially filled with sulfur slightly adsorbed on the mesopore wall in the case of pOMC-S composite. Interestingly, the rOMC-S and sOMC-S composites have densely sulfur-loaded shells on the surface, which correspond to heavily sulfur-loaded zones, which cannot be seen in pOMC-S. Due to this and relatively lower surface area of rOMC and sOMC compared to that of pOMC, the rOMC-S and sOMC-S composites suffer from severe decrease of surface area and pore volume compared to the pOMC-S for identical 60 wt% S loading. In particular, the rOMC-S composite has large trapped dead pore area in deep inner part of the porous framework not accessible by N_2 gas since this has much longer mesopore channels, which cannot be filled with sulfur. This is in full agreement with TEM image of rOMC-S composite in Figure 2a. The densely sulfur-loaded shell on the surface may black the way to inner part, eventually creating trapped dead volume in the inner part. This will decrease the effective usage of surface area and pores for porous carbons with long mesopore channels. Therefore, the pOMC with short mesopore channels has advantages of higher surface area and larger pore volume and can realize much better effective usage of the surface area and pores for sulfur loading because of easy filling of short mesopores, which can eventually facilitate adsorption of more polysulfides, and enhance Li storage capacity with improved rate capability.

Eelectrochemical performance.—To better understand the effects of OMC materials with different mesopore channels, the electrochemical performances of all the OMC-S composite electrodes were investigated. Figure 4a shows the cyclic voltammograms (CVs) of pOMC-S at a scan rate of 0.1 mV s^{-1} in the voltage range of 1.8 to 2.8 V vs. Li/Li^+ for the first five cycles. During the first cathodic process, two reduction peaks are observed at 2.3 V and 2.0 V. According to the earlier reports,[37,38] the peak at 2.3 V corresponds to the reduction of elemental S to soluble lithium polysulfide (Li_2S_x, $4 \leq x < 8$), while the peak at 2.0 V involves further reduction of the lithium polysulfides to insoluble Li_2S_x ($x = 1, 2$). In the subsequent anodic scan, two oxidation peaks are also observed at 2.33 V and 2.4 V, which are attributed to the conversion of Li_2S to the lithium polysulfides and further the short-chain polysulfides to long-chain polysulfides, respectively, indicating good reversibility of the electrode cycling processes.[14] Compared with rOMC-S and sOMC-S in Figure S3, both the CV peak position and area remain almost unchanged after the second cycle, suggesting relatively good capacity retention in pOMC-S composite.

Figure 4b shows the first charge-discharge curves for various OMC-S composites at 0.1 C rate (1 C = 1680 mA g^{-1}). Two discharge plateaus at ~2.3 V and ~2.1 V are observed, which are in agreement with two cathodic peaks in the CV curves.[39] The initial discharge capacity of the pOMC-S cathode is as high as 1419 mAh g^{-1}, corresponding to 84.7% utilization of S with a high initial Coulombic efficiency of 90.4%. In contrast, the rOMC-S and sOMC-S composites show a bit lower initial discharge capacity of 1252 and 1315 mAh g^{-1}, which correspond to 74.7 and 78.5% S utilization based on the theoretical capacity of 1675 mAh g^{-1}, with initial Coulombic efficiencies of 83.7 and 87.8%, respectively, probably because of less efficient mass transfer and polysulfide retention in the rOMC and sOMC.[40] The high discharge capacity in the pOMC-S can be directly correlated with larger surface area and pore volume and better utiliztion of pore poperties associated with short pore channels favoarble for facile mass transfer of active materials.

In Figure 4c, the rate performances were investigated by cycling the cells at various current rates from 0.1 C (168 mA g^{-1}) to 2 C (3360 mA g^{-1}). All the as-synthesized OMCs demonstrate an excellent rate capability, delivering a high fraction of its total capacity even at a rate of 2 C (i.e., 174, 309, and 595 mAh g^{-1} at 3360 mA g^{-1} for rOMC-S, sOMC-S, and pOMC-S, respectively). The 35.5% sulfur utilization of pOMC-S based on the theoretical capacity of sulfur is much higher than those of rOMC-S (i.e., 10.4%) and sOMC-S (i.e., 18.4%) at a rate of 2 C. When the current density was return to a low rate (0.1 C) after cycling at various rates, the pOMC-S recovered a specific capability of 1016 mAh g^{-1} (i.e., 28% decrease) better than rOMC-S (590 mAh g^{-1}, i.e., 58% decrease) and sOMC-S (803 mAh g^{-1}, i.e., 43% decrease), respectively. This indicates that pOMC-S is found to better keep its integrity not only for a long number of cycles but also at high rates.

Figure 4d shows the galvanostatic cycling performance for various OMC-S cells at 168 mA g^{-1}. All the OMC-S cells exhibit relatively fast capacity fading in the intial cycles because the sulfur particles encapuslted in the OMC framework are dissolved and diffused into electrolyte during the cycles, which can lead to the capacity drop due to loss of active sulfur species. After the intial 20 cycles, the sulfur particles are redistributed on the pore of OMC framework and lead to relatively reversible and stable electrochemical reaction. After

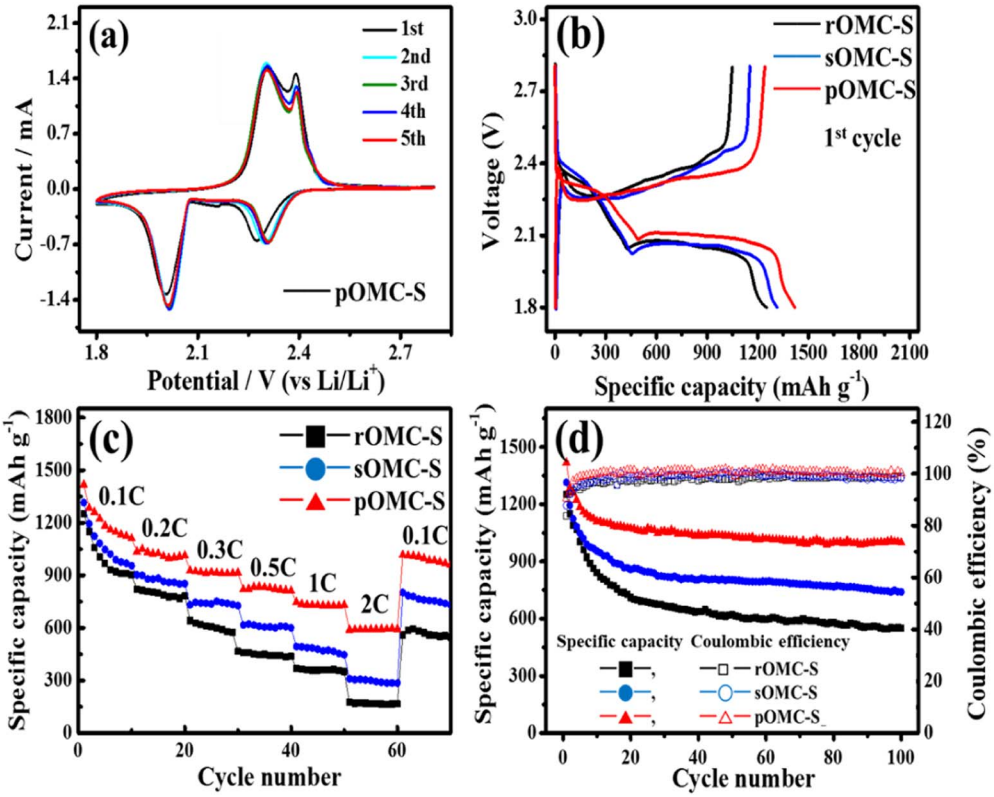

Figure 4. (a) Cyclic voltammogram of pOMC-S composite in a coin cell at a scan rate of 0.1 mV s^{-1} in potential window from 1.8 to 2.8 V vs. Li^+/Li^0. (b) Comparison of galvanostatic charge-discharge curves of various OMC-S cells at a current density of 0.1 C. (c) Rate capabilities of the OMC-S cells at different discharge currents. (d) Cyclic performance at a constant current rate of 0.1 C and the corresponding Coulombic efficiency of OMC-S composites with different channel length.

100 cycles, the pOMC-S cathode retains a capacity of 1002 mAh g^{-1} with an average decay rate of 0.22% per cycle and Coulombic efficiency of 99%, which corresponds to 78.3% capacity retention of initial capacity measured at the second cycle, revealing the highest capacity and the cycling stability among the OMC-S composites. Meanwhile, the rOMC-S and the sOMC-S deliver a capacity of 551 mAh g^{-1} and 740 mAh g^{-1} corresponding to 49.0 and 62.2% capacity retention from the second cycle, with an average decay rate of 0.51 and 0.38% per cycle and Coulombic efficiency of approximately 97%, respectively.

In addition, to check the redox behavior and reversibility of OMC-S cells, cyclic stability was conducted at a higher current density of 2 C for 100 cycles as shown in Figure S4a. The rOMC-S, sOMC-S, and pOMC-S cells show the initial specific capacities of 452, 527, and 721 mAh g^{-1}, respectively. After 100th cycle, the capacities remained at 160, 284, and 502 mAh g^{-1} with capacity retentions of 35, 54, and 70%, respectively. The result indicates that pOMC with high surface area and shorter mesopore channel provides the excellent mass transfer and facilitates the transport of Li ion in the pOMC framework. After the 100 cycles, the CV curves of all the OMC-S cells were measured between 1.8 V and 2.8 V at 0.1 mV s^{-1} for 5 cycles as shown in Figure S4b-d. In comparison to rOMC-S and sOMC-S, pOMC-S shows the well-defined redox reaction peaks, indicating excellent electrochemical reversibility even after 100 cycles at high C-rate. Cycling performance depends on reversible diffusion of lithium ion within porous carbon electrode materials. Short channel length reduces the travel path, favors the unhindered mass transfer, and guarantees effective usage of surface area and pores during insertion/extraction of lithium, thereby increasing capacity retention ability in the order of rOMC-S < sOMC-S < pOMC-S. This is in full agreement with TEM images and N_2 isotherm data for the OMC-S composites with different mesopore channel length.

The electrochemical impedance spectroscopy (EIS) measurements were further performed to investigate the internal resistance of different OMC-S cathodes at fully charged condition, and the corresponding Nyquist plots are shown in Figure 5 with an equivalent circuit diagram presented in an inset. It can be seen that all the Nyquist plots are composed of two semicircles in the middle-high frequency region, and sloping lines in the low frequency region correspond to the Li^+ diffusion within the electrodes.[41] All the OMC-S electrodes show

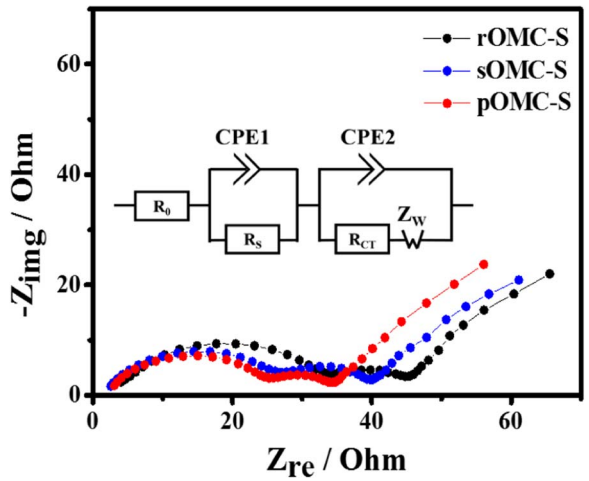

Figure 5. Nyquist plots for various OMC-S composites after 50 cycles at fully charged condition to 2.8 V. The inset is an equivalent circuit used to fit the impedance spectra.

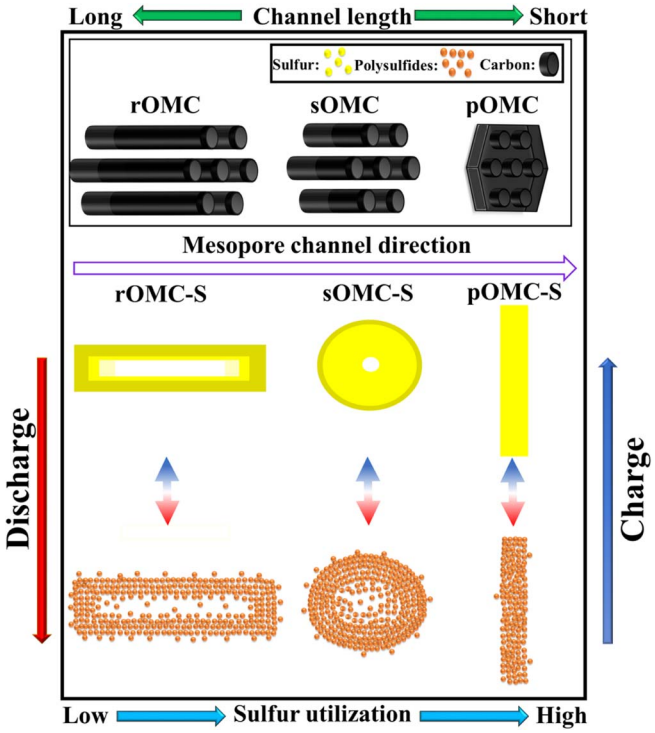

Figure 6. Schematic illustration of sulfur distribution in various OMC-S composites including densely sulfur-loaded shell marked with dark yellow and polysulfide distribution during discharge-charge processes in the OMC-S cathodes for LSB.

similar ohmic resistance (R_o) from high frequency intercept, which corresponds to ionic resistances of electrolyte and contact resistance at the interface between electrodes and current collectors. The semicircle at high frequency region is related to solid electrolyte interface (SEI) film formed on the surface of electrodes (R_s) and the middle frequency semicircle is attributed to the charge-transfer resistance (R_{ct}). R_s values of the OMC-S composites decrease with decreasing mesopore channels from 8.2 Ω (i.e., rOMC-S) to 7.5 Ω (i.e., sOMC-S) and further to 4.9 Ω (i.e., pOMC-S). Furthermore, much smaller R_{ct} value was measured for pOMC-S (i.e., 24.3 Ω) compared to those for its peers, sOMC-S (i.e., 27.9 Ω) and rOMC-S (i.e., 32.5 Ω) with longer channel length. This result may be due to relatively large mesopore volume and short mesopore channels of the pOMC structure, which allow fast charge transport path for both electron and Li ion during discharge and charge cycles. By comparison, in the case of sOMC-S and rOMC-S, dense sulfur loading zone as well as long travel distance will make it slow for active sulfer to interact with Li, increasing the R_{ct}. The unique pOMC nanostructure with short ordered mesopores can provide faster charge and mass transfer in lithium insertion/extraction processes and facile charge transfer at the electrode/electrolyte interface. Eventually, among the OMC-S composites, the pOMC-S shows the lowest R_s and R_{ct} values because of its highly conductive porous host and shortest mesochannel length, facilitating the interface charge and electron transfer. The detailed kinetic parameters derived from the Nyquist plots for the OMC-S composites are summarized in Table S1.

Figure 6 depicts comparative effects of mesopore channel length on the electrochemical performance for each of OMC-S composites as a cathode in LSB. In the OMC-S composite structure, the majority of sulfur is infiltrated into the mesopores with some sulfur on the surface of OMC. The OMC materials with long mesopore channels have heavily sulfur-loaded zone near on the surface as shown in TEM images in Figure 2. The heavily sulfur-loaded zone near on the surface may also black the way to inner part so that densely sulfur-loaded shell and empty or less-populated core zone may form for the rOMC-S and sOMC-S composites. In fact, the rOMC-S composite with longest mesopore channels can have trapped dead volume in the inner part. The thickness of the heavily sulfur-loaded zone increases with increasing mesopore channel length due to difficulty of sulfur in traveling into the inner part with increasing channel length. On the other hand, for pOMC-S with short mesopore channel length, no such heavily sulfur-loaded zone is seen in the composite since sulfur can easily infiltrate the short mesopore channel with more homogeneous sulfur distribution in the pOMC-S composite. Figure 6 shows schematic illustration of sulfur distribution in various OMC-S composites with different yellow grades including densely sulfur-loaded shell marked with dark yellow along with possible empty zone on the basis of experimental evidence.

The discharge-charge processes in the OMC-S cathodes for LSB are also illustrated in Figure 6. During the electrochemical discharge-charge processes, it is also likely that the more polysulfides generated during cycles are located homogeneously throughout the short mesopore channels of pOMC-S due to relative easy filling. The longer the mesopore channels, the less mesopore channels will be filled with the polysulfides also due to increasing transfer resistance. Eventually, the less efficient utilization of mesopore surface area and volume in the OMC with long mesopore channels will induce gradually more polysulfides to be located near on the surface for rOMC-S and sOMC-S compared to pOMC-S. Therefore, the diffusion or shuttle of the soluble polysulfides gets more severe with increasing mesopore length in the OMC-S composites, which will result in less sulfur utilization and thus, less cycle and rate capability in rOMC-S and sOMC-S cathodes. After all, short mesopore channels, which guarantee more homogenous distribution of the polysulfides in the mesopores, help to provide much better electron and ion transport path and mitigate polysulfide diffusion/shuttle during the cycles within the electrode, which can result in a higher sulfur utilization and longer cycle life.

Conclusions

In this study, the OMCs with different mesopore channel length were fabricated and explored as hosts for sulfur as cathode materials in LSB. The mesopore channel length of the OMC host for sulfur has significnat influence not only on mass transfer but also on the sulfur untilization and eventually LSB performance including cycle and rate capabilty of the cell. The as-synthesized OMC-S composites cannot only lead to facile mass transport but also hold soluble polysulfides in the OMC framework because of distinctive structural features such as well-developed 3D conductive hexagonal mesopores, high specific surface area, and large mesopore volume. In particular, thin hexagonal prism-shaped pOMC-S with the short mesopore channels has demonstrated higher sulfur utilization and thus better cycling performance and rate capability compared to the other OMC-S composites with longer mesopore channels. This superb behavior is attributed to more full utilization of mesopore channels for sulfur loading and polysulfide holding, thus demonstrating better LSB performance. We believe that this systematic study will help to better understand the correlation between porous surface structures and LSB performance which is much needed to develop high energy LSB in accordance with present-day requirement.

Acknowledgments

This work was supported by Global Frontier R&D Program on Centre for Multiscale Energy System (NRF-2011-0031571) and (NRF-2016M1A2A2937137) funded by the Ministry of Education, Science and Technology through the National Research Foundation of Korea. The authors also thank Korean Basic Science Institute at Jeonju for SEM, UHR-SEM and TEM analysis.

ORCID

Seongpil Hwang https://orcid.org/0000-0003-4316-194X
Jong-Sung Yu https://orcid.org/0000-0002-8805-012X

References

1. J. B. Goodenough, *Energy Environ. Sci.*, **7**, 14 (2014).
2. Y. Wang and G. Cao, *Adv. Mater.*, **20**, 2251 (2008).
3. L. Xiao, Y. Cao, J. Xiao, B. Schwenzer, M. H. Engelhard, L. V. Saraf, Z. Nie, G. J. Exarhos, and J. Liu, *Adv. Mater.*, **24** 1176 (2012).
4. C. Zhao, L. Liu, H. Zhao, A. Krall, Z. Wen, J. Chen, P. Hurley, J. Jiang, and Y. Li, *Nanoscale*, **6**, 882 (2014).
5. W. J. Chung, J. J. Griebel, E. T. Kim, H. Yoon, A. G. Simmonds, H. J. Ji, P. T. Dirlam, R. S. Glass, J. J. Wie, N. A. Nguyen, B. W. Guralnick, J. Park, P. Theato SomogyiÁrpád, M. E. Mackay, Y.-E. Sung, K. Char, and J. Pyun, *Nat Chem.*, **5**, 518 (2013).
6. Y.-X. Wang, L. Huang, L.-C. Sun, S.-Y. Xie, G.-L. Xu, S.-R. Chen, Y.-F. Xu, J.-T. Li, S.-L. Chou, S.-X. Dou, and S.-G. Sun, *J. Mater. Chem.*, **22**, 4744 (2012).
7. K. Xi, S. Cao, X. Peng, C. Ducati, R. Vasant Kumar, and A. K. Cheetham, *Chem. Commun.*, **49**, 2192 (2013).
8. X. Jia, C. Zhang, J. Liu, W. Lv, D.-W. Wang, Y. Tao, Z. Li, X. Zheng, J.-S. Yu, and Q.-H. Yang, *Nanoscale*, **8**, 4447 (2016).
9. Y. Yang, G. Yu, J. J. Cha, H. Wu, M. Vosgueritchian, Y. Yao, Z. Bao, and Y. Cui, *ACS Nano*, **5**, 9187 (2011).
10. X. Ji, K. T. Lee, and L. F. Nazar, *Nat Mater.*, **8**, 500 (2009).
11. Y. V. Mikhaylik and J. R. Akridge, *J. Electrochem. Soc.*, **151**, A1969 (2004).
12. M. Rao, X. Song, H. Liao, and E. J. Cairns, *Electrochim. Acta*, **65**, 228 (2012).
13. L. Ji, M. Rao, S. Aloni, L. Wang, E. J. Cairns, and Y. Zhang, *Energy Environ. Sci.*, **4**, 5053 (2011).
14. G. Zhou, D.-W. Wang, F. Li, P.-X. Hou, L. Yin, C. Liu, G. Q. Lu, I. R. Gentle, and H.-M. Cheng, *Energy Environ. Sci.*, **5**, 8901 (2012).
15. S.-C. Han, M.-S. Song, H. Lee, H.-S. Kim, H.-J. Ahn, and J.-Y. Lee, *J. Electrochem. Soc.* **150**, A889 (2003).
16. F. Wu, J. Chen, L. Li, T. Zhao, and R. Chen, *J. Phys. Chem. C*, **115**, 24411 (2011).
17. J. Schuster, G. He, B. Mandlmeier, T. Yim, K. T. Lee, T. Bein, and L. F. Nazar, *Angew. Chem. Int. Ed.*, **51**, 3591 (2012).
18. N. Jayaprakash, J. Shen, S. S. Moganty, A. Corona, and L. A. Archer, *Angew. Chem. Int. Ed.*, **50**, 5904 (2011).
19. C. Liang, N. J. Dudney, and J. Y. Howe, *Chem. Mater.*, **21**, 4724 (2009).
20. H. Wang, Y. Yang, Y. Liang, J. T. Robinson, Y. Li, A. Jackson, Y. Cui, and H. Dai, *Nano Lett.*, **11**, 2644 (2011).
21. L. Yin, J. Wang, F. Lin, J. Yang, and Y. Nuli, *Energy Environ. Sci.*, **5**, 6966 (2012).
22. F.-F. Zhang, X.-B. Zhang, Y.-H. Dong, and L.-M. Wang, *J. Mater. Chem.*, **22**, 11452 (2012).
23. X. Jia, C. Zhang, J. Liu, W. Lv, D.-W. Wang, Y. Tao, Z. Li, X. Zheng, J.-S. Yu, and Q.-H. Yang, *Nanoscale*, **8**, 4447 (2016).
24. G. Zheng, Y. Yang, J. J. Cha, S. S. Hong, and Y. Cui, *Nano Lett.*, **11**, 4462 (2011).
25. Y. Yang, G. Zheng, and Y. Cui, *Chem. Soc. Rev.*, **42**, 3018 (2013).
26. D. Li, F. Han, S. Wang, F. Cheng, Q. Sun, and W.-C. Li, *ACS Appl. Mater. Interfaces*, **5**, 2208 (2013).
27. J. Fan, C. Yu, L. Wang, B. Tu, D. Zhao, Y. Sakamoto, and O. Terasaki, *J. Am. Chem. Soc.*, **123**, 12113 (2001).
28. S. B. Yoon, J. Y. Kim, and J.-S. Yu, *Chem. Commun.*, **0**, 559 (2001).
29. B. Fang, J. H. Kim, M.-S. Kim, and J.-S. Yu, *Acc. Chem. Res.*, **46**, 1397 (2013).
30. S. Kang, Y. B. Chae, and J.-S. Yu, *Nanosci. Nanotechnol.*, **9**, 527 (2009).
31. S.-Y. Chen, C.-Y. Tang, W.-T. Chuang, J.-J. Lee, Y.-L. Tsai, J. C. C. Chan, C.-Y. Lin, Y.-C. Liu, and S. Cheng, *Chem. Mater.*, **20**, 3906 (2008).
32. D.-S. Yang, D. Bhattacharjya, M. Y. Song, and J.-S. Yu, *Carbon*, **67**, 736 (2014).
33. D. S. Yang, D. Bhattacharjya, S. Inamdar, J. Park, and J.-S. Yu, *J. Am. Chem. Soc.*, **134**, 16127 (2012).
34. M.-S. Kim, D. Bhattacharjya, B. Fang, D.-S. Yang, T.-S. Bae, and J.-S. Yu, *Langmuir*, **29**, 6754 (2013).
35. G.-L. Xu, Y.-F. Xu, J.-C. Fang, X.-X. Peng, F. Fu, L. Huang, J.-T. Li, and S.-G. Sun, *ACS Appl. Mater. Interfaces*, **5**, 10782 (2013).
36. K. Jin, X. Zhou, L. Zhang, X. Xin, G. Wang, and Z. Liu, *J. Phys. Chem. C*, **117**, 21112 (2013).
37. X. Ji and L. F. Nazar, *J. Mater. Chem.*, **20**, 9821 (2010).
38. L. Ji, M. Rao, H. Zheng, L. Zhang, Y. Li, W. Duan, J. Guo, E. J. Cairns, and Y. Zhang, *J. Am. Chem. Soc.*, **133**, 18522 (2011).
39. G. Zhou, L.-C. Yin, D.-W. Wang, L. Li, S. Pei, I. R. Gentle, F. Li, and H.-M. Cheng, *ACS Nano*, **7**, 5367 (2013).
40. J. Yang, J. Xie, X. Zhou, Y. Zou, J. Tang, S. Wang, F. Chen, and L. Wang, *J. Phys. Chem. C*, **118**, 1800 (2014).
41. N. A. Cañas, K. Hirose, B. Pascucci, N. Wagner, K. A. Friedrich, and R. Hiesgen, *Electrochim. Acta*, **97**, 42 (2013).